

CFD Predictions of Control Effectiveness for a Generic Highly Swept UCAV Configuration

Joe Coppin¹ and Trevor Birch²

Defence Science and Technology Laboratory, Fareham PO17 6AD, U.K.

A computational study has been completed into the transonic aerodynamics of a generic highly swept UCAV configuration with particular attention to the prediction of the effectiveness of a range of trailing edge controls using an automated mesh generation tool and Reynolds averaged Navier-Stokes solver. Computational results are compared with data from wind tunnel tests over the Mach number range $0.5 \leq M \leq 0.9$ for the case with no control deflections. Results for several different trailing edge controls are then presented and compared with experimental data for a Mach number of 0.7. The computational results provide additional insight into the underlying flow physics.

Nomenclature

C_L	= lift coefficient
C_D	= drag coefficient
C_x	= axial force coefficient
C_y	= side force coefficient
C_z	= normal force coefficient
C_l	= rolling moment coefficient (based on semispan)
C_m	= pitching moment coefficient (based on aerodynamic mean chord)
C_n	= yawing moment coefficient (based on semispan)
$C_{n\beta}$	= directional stability $\partial C_n / \partial \beta$
$C_{m\alpha}$	= directional stability $\partial C_m / \partial \alpha$
C_p	= pressure coefficient
M_∞	= free-stream Mach number
q_∞	= free-stream dynamic pressure (pa)
p_∞	= free-stream static pressure (pa)
T	= Temperature ($^\circ\text{K}$)
Re	= Reynolds number (based on aerodynamic mean chord)
y^+	= non-dimensional boundary layer parameter, $y^+ = yu_\tau / \nu$
ν	= kinematic viscosity (m^2/s)
α	= angle of incidence (positive nose up)
β	= angle of sideslip (wind from starboard)
Λ	= leading edge sweep
S_{ref}	= reference area (planform area) (m^2)
c_{ref}	= reference chord (aerodynamic mean chord) (m)
b_{ref}	= reference span (semispan) (m)

Acronyms:

SACCON	Stability And Control CONfiguration
UCAV	Unmanned Combat Air Vehicle
HSWT	High Speed Wind Tunnel (BAE-Systems Warton)
IB	Inboard (Flap)
OB	Outboard (Flap)

¹ Aerodynamicist, Air and Weapons Systems Department, DSTL

² Aerodynamics Fellow, Air and Weapons Systems Department, DSTL, Senior Member AIAA

RANS Reynolds Averaged Navier-Stokes
 MRP Moment Reference Point

I. Introduction

The design and analysis of the aerodynamic control effectors of unmanned combat air vehicles (UCAVs) is currently of significant interest. The NATO STO task group AVT-201 was established with the objective of determining a strategy for creating stability and control (S&C) databases for air vehicle simulation¹. Under a previous study (AVT-161), the SACCON (Stability And Control CONfiguration) concept was developed to provide a relevant test case and it has been extensively studied in a number of countries both experimentally and computationally. Until recently much of the work in AVT-201 and AVT-161 was focused on investigating the low speed static and dynamic characteristics of the SACCON concept².

This paper aims to widen this assessment into the transonic range and presents results from a CFD study and compares them with wind tunnel data. The approach adopted involves the use of engineering CFD. Typically the bottleneck for viscous flow CFD is mesh generation. Here the burden has been significantly reduced through the use of a scriptable automated unstructured mesh generator.

Predicted forces and moments for the baseline configuration and the configuration with various trailing edge controls are presented and compared with wind tunnel data. Computed surface pressure distributions and skin friction lines are also presented to give insight into the underlying flow physics and improve our understanding of the forces and moments.

A. Model Description

1. Basic Configuration

The SACCON configuration shown in Figure 1 is a highly swept ($\Lambda=\pm 53^\circ$) lambda wing UCAV with parallel leading and trailing edges. Design of the SACCON configuration is detailed in Reference 5. The leading edge has a varying radius, sharp at the root and transitioning to round at the first crank and for the remainder of the wing. The root section is 12.5% thick so that the centre-body can house the intake, engine, and internal components, and then the wing is 12% thick at the first crank, reducing to 7.3% at the second crank. The chord reduces to zero at the wingtip. There is also 5° of washout applied between the first and second cranks. The reference values used in this paper are consistent with those used for the high speed wind tunnel tests. The reference chord is based on the aerodynamic mean chord and the moment reference point is at the planform neutral point. Note that these are different from other values used in the low speed tests for AVT-161 and AVT-201.

Reference area	S_{ref}	=	0.1173m ²
Reference chord	c_{ref}	=	0.23424m (aerodynamic mean chord)
Reference span	b_{ref}	=	0.3m (semispan)
Moment reference point	$(x,y,z)_{ref}$	=	0.21204, 0, 0m (from the nose)

2. Controls

The SACCON F17E wind tunnel model has cut-out trailing edges on the port and starboard sides to allow controls to be fitted. There is provision for two flaps on each wing between the first and second cranks labelled IB (inboard) and OB (outboard) as shown in Figure 4. The cut-out is approximately 20% of the local chord and the equivalent hinge line lies in approximately this location. In the inboard position, plain flaps, $+10^\circ$, 0° and -10° can be fitted. In the outboard position, plain flaps ($+10^\circ$, 0° and -10°) or a split flap ($\pm 10^\circ$ or $\pm 20^\circ$) can be fitted. These flaps configured in various combinations are intended to give pitch, roll and yaw control to the vehicle. Throughout the wind tunnel test, controls were primarily fitted to the port wing with some cases having controls on both sides to test for interference. For the CFD test cases only port controls are considered. The flaps are attached to the wing in such a way that there is no gap present at the control root in the undeflected or deflected states.

B. Experimental Overview

1. Description of Facility

The SACCON F17E model has been tested in the DNG-TWG^{3,6} wind tunnel in Göttingen Germany and in the BAE-Systems HSWT in Lancashire, UK^{3,4}. For this study, only results from the HSWT are considered. The BAE-Systems HSWT is an intermittent blowdown tunnel with a 1.2 x 1.2m test section with run times of up to 30s. It can either be used in a transonic ($0.4 < M < 1.14$) or supersonic ($1.4 < M < 3.8$) regime but for the SACCON test, Mach numbers in the range $0.5 < M < 0.9$ were tested.

2. Transition Fixing

Boundary layer transition was fixed in the experiment using the ‘Boeing Dot’ method⁴ as shown in Figure 2. The dots were supplied as pre punched adhesive tape and placed 3.2mm behind the leading edge on the upper and lower surfaces. The dot height was $183\mu\text{m}$, the diameter was approximately 1.25mm and the dots were placed 1.25mm apart. The majority of runs had transition fixed in this way but some runs were completed with free transition.

3. Flow Conditions

In the HSWT experiment, the reservoir total pressure was nominally set to 138Kpa and the desired Mach number was set using the 2nd throat. There is also a Mach flap system in the tunnel to compensate for model blockage. Total pressure (p_t), dynamic pressure (q_{inf}) and Reynolds number (Re) were recorded for each point. Run averaged values were used to derive the free-stream conditions for the CFD calculations. These values are given in Table 1 for the selected test cases. The freestream conditions for the undeflected clean configuration at zero sideslip were used for all of the corresponding CFD calculations to provide consistency.

4. Measurements

The SACCON F17E model was mounted on a 6 component internal balance connected to a rear sting. The test comprised mainly of force and moment runs at fixed Mach numbers in continuous sweep mode, where the model incidence was varied. Some data was also acquired in pitch pause mode, where model incidence was fixed.

II. Description of the CFD Test Cases

A. Clean Configuration (no control deflections)

CFD test cases for the clean configuration consist of alpha polars ($-3^\circ \leq \alpha \leq 18^\circ$), ($\beta=0, -5$) at Mach numbers 0.5, 0.7, 0.8 and 0.9. The specific details are shown in Table 1.

Mach	Alpha (°)	Beta (°)	Run No. TFixed	Run No. TFree	q_{inf} (kPa)	Re/m	p_{inf} (kPa)	T_{inf} (°K)
0.5	Trav	0	R264-0059	R264-0241	20.37	14.35	116.2	272.6
0.5	Trav	-5	R264-0042					
0.7	Trav	0	R264-0047	R264-0240	34.09	18.81	99.41	254.1
0.7	Trav	-5	R264-0049					
0.8	Trav	0	R264-0208		40.59	19.61	90.56	254.0
0.8	Trav	-5	R264-0207					
0.9	Trav	0	R264-0058	R264-0239	46.35	20.68	81.66	246.5
0.9	Trav	-5	R264-0053					

Table 1 CFD test cases clean configuration

B. Deflected Controls

In the experiment, all control configurations were tested at $M=0.5$, 0.7 and 0.9 . However in this study we have only considered the $M=0.7$ case. This was done to avoid overlap with other AVT-201 participant's work on controls at low speed⁷ and to avoid the higher Mach number case ($M=0.9$) where the characteristics of the basic configuration were poor, featuring strong shockwaves and trailing-edge separation. In addition, at $M=0.7$, a wide range of flows are observed over the incidence range ($\alpha=0-20^\circ$). A summary of the test cases is given in Table 2. Individual deflections for each flap are included as well as combined differential deflections, known as crow flaps. The sign convention for flap deflections is positive for trailing edge down deflections as shown in Figure 3.

	IB Flap	OB Flap	HSWT Run No	Mach Number	Alpha, Beta
Config. 0	0	0	R264-0047	0.7	$\alpha=0-20^\circ$, $\beta=0$
Config. 1	+10	0	R264-0078	0.7	$\alpha=0-20^\circ$, $\beta=0$
Config. 2	-10	0	R264-0071	0.7	$\alpha=0-20^\circ$, $\beta=0$
Config. 3	0	+10	R264-0099	0.7	$\alpha=0-20^\circ$, $\beta=0$
Config. 4	0	-10	R264-0104	0.7	$\alpha=0-20^\circ$, $\beta=0$
Config. 5	0	Split ± 10	R264-0092	0.7	$\alpha=0-20^\circ$, $\beta=0$
Config. 6	+10	-10	R264-0140	0.7	$\alpha=0-20^\circ$, $\beta=0$
Config. 7	-10	+10	R264-0127	0.7	$\alpha=0-20^\circ$, $\beta=0$

Table 2 CFD test cases controls

III. Computational Methods

A. Geometry and CAD

The geometry used for the CFD calculations is based on the F17E wind tunnel model CAD which was supplied to the AVT-201 group in a number of CAD parts. The first supplied CAD file contained the baseline configuration with cut outs for the control surfaces and a truncated sting. This file was modified in two ways; the sting was truncated with a tangent ogive rather than a hemisphere to reduce the risk of convergence problems, and the gaps around the edges of the control surfaces and wing cut-outs were filled to avoid holes in the geometry when the control surfaces were deflected. Separate CAD files for each control surface at each deflection angle were also extracted from the supplied files, inboard, and outboard flaps at -10 , 0 and $+10^\circ$. The split flap geometry was produced by importing the OB flaps at $+10$ and -10° as no CAD was available. There was no need to intersect components or remove internal surfaces as this was not required by the mesh generator.

B. Mesh generation

Two different mesh generators were used in this study. Firstly for the clean aircraft, ICEM TETRA and PRISM were used to generate a predominantly tetrahedral mesh with prism layers to resolve the boundary layer. The farfield was placed >20 semi-spans from the UCAV and the 1st cell height was set to give a $y^+O(1)$. The resulting mesh size was 14 Million cells for the full aircraft. This mesh is shown in Figure 6.

The second set of meshes (example in Figure 7) was used to investigate the incremental forces and moments from control deflections. These were generated using BOXERMesh, which enables straightforward meshing around complex configurations with minimal effort spent manipulating CAD. These meshes comprised predominantly of hexahedral cells with prism layers near the walls. The mesh generator was scripted so that meshes could be automatically generated and each configuration was successfully meshed without user intervention. These meshes are all half models (symmetry) and are relatively large compared with the ICEM meshes with similar surface spacing. This is mainly because the mesh is not permitted to grow away from the surface as quickly as is possible for tetrahedral meshes. Furthermore, a finer surface mesh is also required to accurately capture the geometry. The half mesh sizes for each configuration were approximately 23 million cells. To assess the grid sensitivity, a coarse (8.8 million) and a fine (64 million) mesh were also generated for configurations 0 and 6. This was done by scaling the farfield mesh size, which controls all other mesh spacings and approximates to isotropic refinement apart from in the normal direction in the prism layer region. For the intermediate mesh the 1st cell height was larger than ideal for low y^+ wall treatment (average $y^+=5.9$). This is due to a cell aspect ratio limit in BOXERMesh. To overcome this

very fine surface mesh would be required which would result in prohibitively large mesh sizes. The average y^+ for the fine mesh was approximately 3.

C. Flow solver

All of the computations carried out used the commercially available unstructured Navier-Stokes flow solver Cobalt⁹ v6.1. Cobalt employs a cell centred finite volume approach and a Godunov exact Riemann solver with least squares reconstruction to provide second-order accuracy. A variety of turbulence models are available in Cobalt although all of the results presented in this paper were obtained using the standard Spalart-Allmaras model⁸.

The majority CFD calculations were run fully turbulent. Some additional CFD runs were completed using the Spalart-Allmaras model with a trip term⁸ in order to simulate the transition fixing used in the wind tunnel test. In this case, strips of cells on the upper and lower surfaces were marked as trip cells in the region $3.2 < x < 6.2$ mm. For the SA model with trip term, the freestream eddy kinematic viscosity is $\nu = 0.1\nu_{mol}$ compared with $\nu = 3.0\nu_{mol}$ for the standard SA model.

Computations were run on the Dstl HPC cluster using 600 cores for 800 iterations each. No convergence problems were encountered and the forces and moments were typically converged to steady state in fewer than 500 iterations. Residual convergence was also checked and the continuity residual typically reduced by over 6 orders.

D. Force reduction

The CFD calculations for cases with deflected controls were completed on half body meshes for the port wing only. In order to obtain force and moment coefficients for the complete configuration to compare with the wind tunnel results, loads from the clean starboard wing were required before computing the coefficients. These were obtained from a clean port wing calculation which was then mirrored. The force coefficients were computed in the following manor.

$$\begin{aligned} C_x &= (F_x + F_{x, clean}) / q_\infty S \\ C_y &= (F_y - F_{y, clean}) / q_\infty S \\ C_z &= (F_z + F_{z, clean}) / q_\infty S \\ C_l &= (M_l - M_{l, clean}) / q_\infty S b_{ref} \\ C_m &= (M_m + M_{m, clean}) / q_\infty S c_{ref} \\ C_n &= (M_n - M_{n, clean}) / q_\infty S b_{ref} \end{aligned}$$

This assumes that the flow on the port and starboard wings are independent. Using half meshes (assuming symmetry) significantly reduces the mesh size and hence computation time to just over half of that required for a full wing.

Control increments for roll, pitch and yaw were calculated by subtracting the force and moment coefficients of the undeflected configuration (Config. 0) from the coefficients of the configuration of interest.

$$\begin{aligned} \Delta C_l &= C_l - C_{l, config0} \\ \Delta C_m &= C_m - C_{m, config0} \\ \Delta C_n &= C_n - C_{n, config0} \end{aligned}$$

IV. Results

In this section the forces and moments and flow visualisation for the clean wing across a range of freestream conditions are presented. This is followed by the incremental forces and moments and associated computational flowfields for cases with deflected controls.

A. Clean Configuration

1. Forces and Moments

Figures 9, 11, 13 and 15 show the lift, drag, pitching moment and directional stability for the clean configuration over the range of Mach numbers computed. In some cases, where available, two sets of experimental data are presented, one transition free and one transition fixed. For each Mach number, lift is accurately predicted up to the stall (flow breakdown). This flow breakdown also leads to abrupt changes in pitching moment and directional stability $C_{n\beta}$. At $M=0.5$, some nonlinear vortex lift is evident between $13^\circ < \alpha < 16^\circ$, indicated by a steepening of the lift curve slope. This phenomenon is not evident at $M \geq 0.7$. At all Mach numbers the incidence at which the wing stalls is over estimated by the CFD, occurring approximately 2° later than indicated in the experiment.

In each case the zero lift drag is over predicted by approximately $\Delta C_D \approx 0.0025-0.003$ accounting for around 30% of the total drag compared with the transition fixed result. There is also a significant difference between the experimental data for transition fixed and transition free. At incidences above $\alpha=12^\circ$ the drag predicted by the CFD is generally closer to that measured in the wind tunnel.

In most cases the pitching moment slope is initially negative, indicating the vehicle is statically stable in pitch about the MRP. The CFD results diverge from the experiment with increasing Mach number. The measured pitching moment characteristics are nonlinear and some significant differences are evident between the transition fixed and free measurements. The predictions are typically more linear than the measured data until just before the pitchup, which is generally predicted to occur at a higher incidence. Results obtained with the SA model with trip term are not significantly different from the standard SA model.

The directional stability is also very important for tailless UCAVs. Here the directional stability $C_{n\beta}$ is calculated using finite differences from polars at $\beta=0^\circ$ and $\beta=\pm 5^\circ$. For the experimental results, C_n was interpolated on to a common grid every 0.5° to enable this calculation. Two experimental $C_{n\beta}$ estimates were computed from runs with positive and negative sideslip, each gives a slightly different result as shown in Figure 9. At all Mach numbers the CFD predicts the directional stability well at low incidence. However once flow breakdown has occurred, the quantitative agreement between measurement and prediction is not so good, although the trends are reasonably well predicted. The $C_{n\beta}$ curves change significantly with Mach number. At the lower transonic Mach numbers ($M=0.5, 0.7$) the wing becomes directionally unstable above $\alpha=8^\circ$, which is earlier than pitchup. At the higher Mach numbers there is a tendency for increased directional stability and at $M=0.9$ the wing is directionally stable across the incidence range.

2. Computational Flow Visualisations

Figures 10 to 13 show computed skin friction lines and C_p on the upper wing surface a selection of freestream Mach numbers and incidence angles. At $M=0.5$ (Figure 10), development of the upper surface flow separation starts at the wingtip with a small region of separated flow and a low pressure region associated with a vortex. At $\alpha=8^\circ$ and above there is also a small separation visible from the apex which reattaches a short distance downstream. At low incidence this does not seem to significantly alter the pressure distributions although the surface streamlines from this separation/reattachment run towards the inboard trailing-edge crank. This may contribute to the trailing-edge separation which is visible at $\alpha=10^\circ$ and $\alpha=12^\circ$. At higher incidence angles, both the tip vortex and the apex separation grow in size and at $\alpha=14^\circ$ there is only a small portion of the leading edge that retains attached flow. At $\alpha=16^\circ$, the two vortices seem to have partially combined although there are still two distinct suction footprints visible in the C_p distribution with the tip vortex appearing stronger. The tip vortex has now moved inboard so much that its influence has reduced at the tip and hence a local loss in lift is seen. At $\alpha=18^\circ$ the two vortices seem to have fully combined generating a larger suction region near the apex. Along with the loss of lift at the wingtip, this explains the pitchup seen in the forces and moments. The flow in the vicinity of the centreline ($y=0$) remains attached throughout the incidence range.

The flow development at $M=0.7$ (Figure 12) is largely similar to that at $M=0.5$ although some effects due to compressibility can be seen. Shock footprints approximately parallel to the leading edges are visible at $\alpha=10^\circ$, although these do not appear to affect the surface flow pattern significantly. At $\alpha=14^\circ$ the apex separation is slightly larger than at $M=0.5$ and the tip vortex is less concentrated, increasing in diameter more quickly and providing less

additional vortex lift. It is unclear whether this is caused by shock interactions or just the increased pressures caused by compressibility. This trend also continues at the higher incidence angles.

At $M=0.8$ (Figure 14) the visible shocks are now stronger and begin to cause local flow separation. There are three main shocks visible on the upper surface of the wing. One mentioned above which runs approximately parallel to the leading edge and a lambda shock system comprising of two shocks partially combining outboard. At $\alpha=10^\circ$ there are three sources of flow separation visible, the apex and tip leading edge separations and a shock induced separation caused by the outboard (combined) part of the lambda shock at approximately 50-70% span. Unlike the leading edge separations, this does not tend to result in strong vortex flows and hence lift is lost. At $\alpha=12^\circ$ and above little vortex lift is seen.

At $M=0.9$ (Figure 16), the wing flow becomes quite different. There is a strong lambda shock, the trailing leg of which extends inboard all the way to the wing root. This forms an arc on the upper surface joining the wingtips and the inboard trailing edge cranks which causes almost all of the trailing edge flow to separate - even at low incidence angles. Additionally, the leading part of the lambda shock causes kinks in the surface flow streamlines when $\alpha \leq 10^\circ$ and flow separation for $\alpha \geq 12^\circ$. These shock separations seem to replace the leading edge separation seen at the lower Mach numbers and they occur at a lower incidence.

B. Deflected Controls (M=0.7)

1. Outboard Flap (+10°, Config. 3 and -10°, Config. 4)

Figure 19 shows the incremental moment coefficients for the outboard flap. At low incidence the flap behaves as expected in both the pitch and roll axes and each deflection provides approximately the same control effectiveness. In the yaw axis, the positively deflected flap creates a positive moment (nose to starboard) and a negative deflection creates a negative moment. These yawing moments are counter intuitive and cannot be explained by the usual arguments about adverse yaw being caused by increased drag. As the incidence is increased, the effectiveness in the pitch and roll axes changes. A positive deflection (trailing edge down) becomes more effective at high incidence whereas the negative deflection (trailing edge up) becomes less effective.

For the outboard flap the control effectiveness predictions approximate the experimental results in all three axes however there are qualitative and quantitative differences. The predicted skin friction lines, shown in figure 20, indicate that for positive flap deflections, the flap upper surface flow is always separated. Negative flap deflections lead to the upper surface flow near the trailing edge staying attached until higher incidence angles. An example of this can be seen at $\alpha=5^\circ$ on Config. 4.

At incidence angles greater than approximately 15° the flap experiences reverse flow from an upstream separation although the influence of the vortex flow is fairly weak in the vicinity of the outboard flap. On the lower surface, the flow stays attached across the incidence range.

2. Inboard Flap (+10°, Config. 1 and -10° Config. 2)

For the inboard flap (Figure 17), the trends are similar to the outboard flap at low incidences. At higher incidences ($15^\circ \leq \alpha \leq 20^\circ$), in the roll and pitch axes, a reduction in control effectiveness is observed. In the yaw axis, at low incidence the moment increments are in the same sense as those of the outboard flap. The moment increments increase in magnitude with increasing incidence before an abrupt control reversal is seen at $\alpha=15^\circ$. At $\alpha=20^\circ$ the control is still reversed but the magnitude of the moment increment has reduced.

The agreement between the numerical predictions and experimental measurements are generally not as good as for the outboard flap. Rolling moment increments are over predicted for both deflections and pitching moment increments are over predicted for the negative deflection. However the control reversal in the yaw axis is predicted.

The computed skin friction lines (Figure 18) show similar features to those seen for the outboard flap, although for the inboard flap the upper surface boundary layers seem to separate more readily. For negative flap deflections the flow on the lower surface stays attached across most of the incidence range. At $\alpha=15^\circ$, the computed skin friction lines show that there is some spanwise flow on the lower surface (Fig 18 Config. 2 $\alpha=15^\circ$). At high incidence ($\alpha \geq 15^\circ$) the tip and apex vortices appear to combine to form a single vortex. This vortex passes relatively close to the inboard flap and could be responsible for the control reversal and large yawing moment increments.

3. Split Flap ($\pm 10^\circ$, Config. 5)

The split flap is primarily a yaw control effector. Figure 21 shows that for $\alpha < 7.5^\circ$, it acts in the correct sense i.e. it develops additional drag, resulting in a negative yawing moment (for a port split flap). The yawing moment generated by the split flap is similar in magnitude to that generated by the outboard plain flap.

At higher incidence ($\alpha \geq 7.5^\circ$), a gradual control reversal is evident in the wind tunnel results. This is followed by a second abrupt control reversal at $\alpha = 15^\circ$. In the roll and yaw axes the moments generated are initially small at low incidence and increase as the incidence is increased. The direction of the moment increments is consistent with a loss in lift on the port wing. The predicted results agree reasonably well with the measured data. However, the predictions were only done at 5° intervals and therefore cannot capture the abrupt changes observed in the measured data.

Figure 23 shows a rear view of the split flap at each incidence angle computed. The surface is coloured by C_p with colours ranging from red ($C_p = 0$) indicating close to static pressure to blue ($C_p = -0.5$) indicating suction (drag). At $\alpha = 0$, there is a relatively small region of suction towards the inboard end of the flap. A short distance outboard the flow attaches and the skin friction lines indicate spanwise flow. The pressure in this region is close to freestream static, indicating that the base drag component of the flap is not significant. This may explain why the split flap is only as effective in the yaw axis as a single plain flap at the same spanwise location. As incidence increases no significant change in pressure on the rear facing split flap surfaces is evident until $\alpha = 20^\circ$ when the upper surface flow on the wing is largely separated.

4. Crow Flaps ($IB+10^\circ OB-10^\circ$, Config. 6 and $IB-10^\circ OB+10^\circ$ Config. 7)

Crow flaps are again primarily intended to be used as yaw controls by generating additional drag forces. Figure 24 shows that the crow flaps are only effective in yaw in the correct sense when $\alpha < 5^\circ$ for Config. 6 and $\alpha < 10^\circ$ for Config. 7. The incremental yawing moment generated by Config. 7 ($IB-10^\circ OB+10^\circ$) is small. Above these incidence angles the yaw controls are reversed and the moments are clearly driven by the inboard flap discussed in section B-2 above. In common with the split flap, both configurations generate pitch and rolling moments consistent with a loss in lift on the port wing.

The trends in the computational results are reasonably well predicted although quantitatively there are differences. The computed surface flow visualisation in Figure 25 shows that the surface flow patterns are similar to those for the individual deflections. A noticeable difference is in a small region on the outboard flap where the wake (a small vortex) from the side edge of the inboard flap can be seen.

5. Mesh Refinement ($IB+10^\circ OB-10^\circ$, Config. 6)

Figure 26 shows the incremental forces for the crow flaps (Config. 6) for three different meshes; a coarse mesh (8.8 million), medium (23 million) and a fine (64 million) mesh. The incremental forces for each mesh are very similar and any differences are much smaller than the differences between the numerical and experimental results.

V. Conclusions

CFD predictions for the SACCON configuration at transonic speeds with and without controls are presented and compared with wind tunnel results. The results show that for the clean aircraft, reasonable predictions of lift, drag, pitching moment and directional stability can be obtained, although there is a tendency to predict stall and pitchup slightly later than in the experiment, especially at higher Mach numbers.

For the cases with deflected controls, control increments and trends in all axes are predicted reasonably well, even though for some conditions the underlying flow is very complex and some of the controls are located in regions of separated flow. Due to the complexity of the flowfields and the fact that only forces and moments were measured in the experiment it is difficult to understand the cause of the deficiencies in the CFD.

The results show that control of the SACCON configuration using the trailing edge controls defined on the F17E model will be challenging. Each control investigated develops significant moments in all three axes and are highly non-linear. At higher incidence angles, none of the yaw control devices are effective and a control reversal is often seen. The CFD results, particularly surface pressure and skin friction plots are a useful aid to understanding the underlying flow physics even though there are quantitative differences in the forces and moments.

Acknowledgments

The work reported here was undertaken as part of a NATO STO collaborative activity. The authors would like to thank Martin Rein from DLR, who provided the wind tunnel model and Glyn Rigby from BAE-Systems who lead the BAE-Systems wind tunnel test.

References

- ¹Cummings, R. M., and Schütte, A., "The NATO STO Task Group AVT-201 on 'Extended Assessment of Stability and Control Prediction Methods for NATO Air Vehicles'," *32nd AIAA Applied Aerodynamics Conference*, AIAA 2014-2000, 2014.
- ²Various Authors, "Assessment of Stability and Control Prediction Methods for NATO Air and Sea Vehicles" RTO-TR-AVT-161 AC/323(AVT-161)TP/440, Final Report, NATO Science and Technology Organization, 2012
- ³Rein, M., Irving, J., Rigby, G. and Birch, T., "High speed static experimental investigations to estimate control device effectiveness and S&C capabilities", *32nd AIAA Applied Aerodynamics Conference*, AIAA 2014-2004, 2014.
- ⁴Fairhurst, D. J., "A Summary of SACCON DLR-F17E Tests Carried out on Model RA234 in the Warton 1.2m High Speed Wind Tunnel", BAE-WEIS-RP-ASF-WTD-119741 WP070-O-005, BAE-Systems, Warton, 2012.
- ⁵Hitzel, S., "Stability and Control Configuration – Aerodynamic Layout for Test Wing", RTO-AVT-161 Internal document.
- ⁶Rein, M., "Measurements of aerodynamic forces and moments on the DLR-F17E model in low- and high-speed flows", DLR Report No. IB 224–2011 A61, 2011.
- ⁷Schütte, A., Huber, K., Boelens, O., "Static and dynamic numerical simulations of a generic UCAV configuration with and without control devices", *32nd AIAA Applied Aerodynamics Conference*, AIAA 2014-2132, 2014.
- ⁸Spalart, P. R. and Allmaras, S. R., "A One-Equation Turbulence Model for Aerodynamic Flows", *AIAA Paper* 92-0439.
- ⁹M. J. Grismer, W. Z. Strang, R. F. Tomaro, and F. C. Witzemman, "Cobalt: A Parallel, Implicit, Unstructured Euler/Navier-Stokes Solver," *Adv. Eng. Software*, Vol. 29, No. 3-6, pp. 365-373, 1998.

Figures

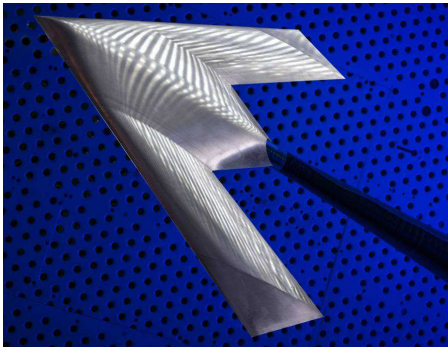


Figure 1: DLR F17E in the 1.2m HSWT

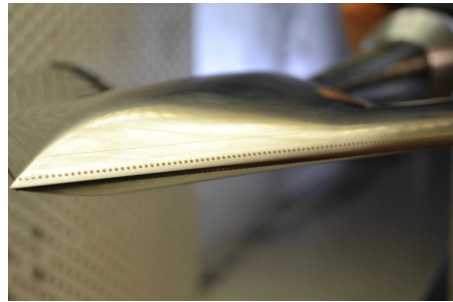


Figure 2 Transition Dots on the F17E

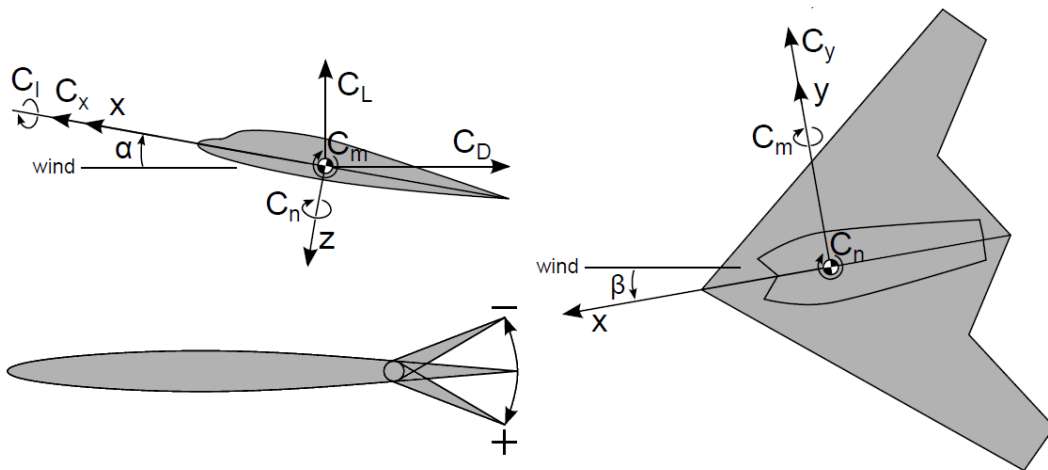


Figure 3: Axes and conventions

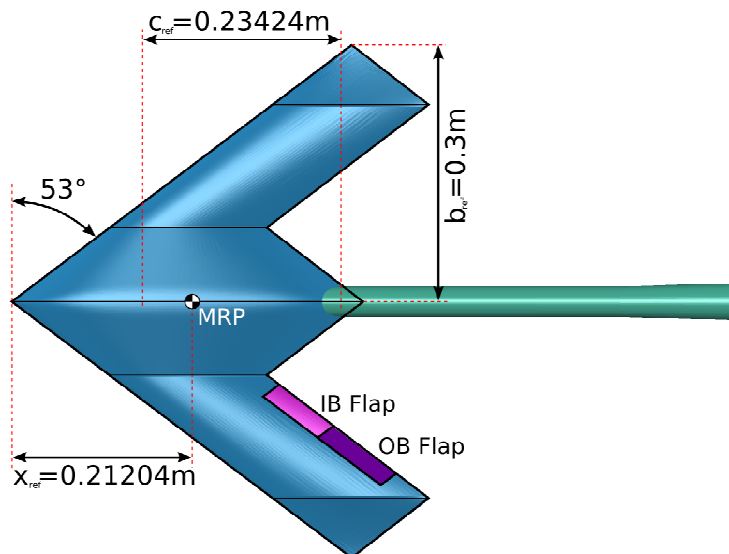


Figure 4: Reference values and notation

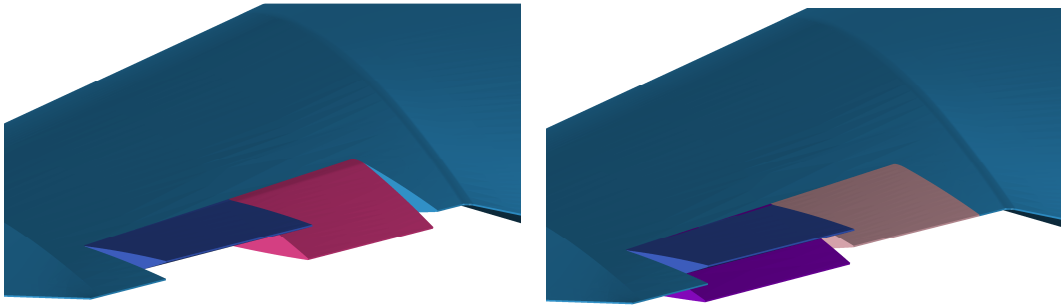


Figure 5: Crow and split flap geometries

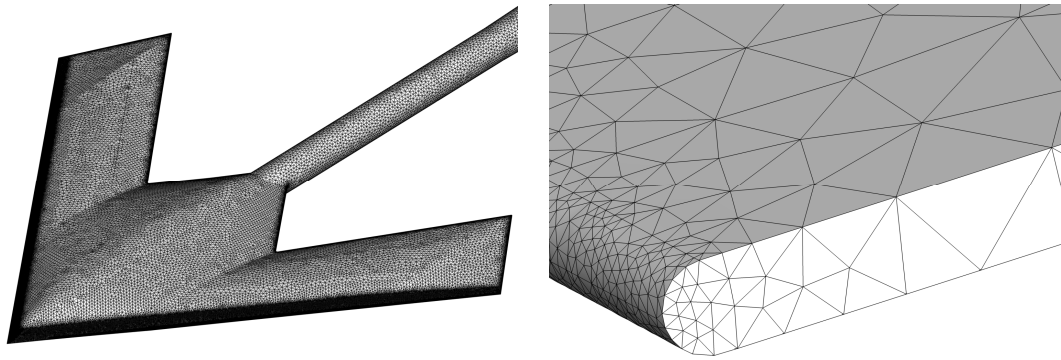


Figure 6: ICEM grid for clean configuration

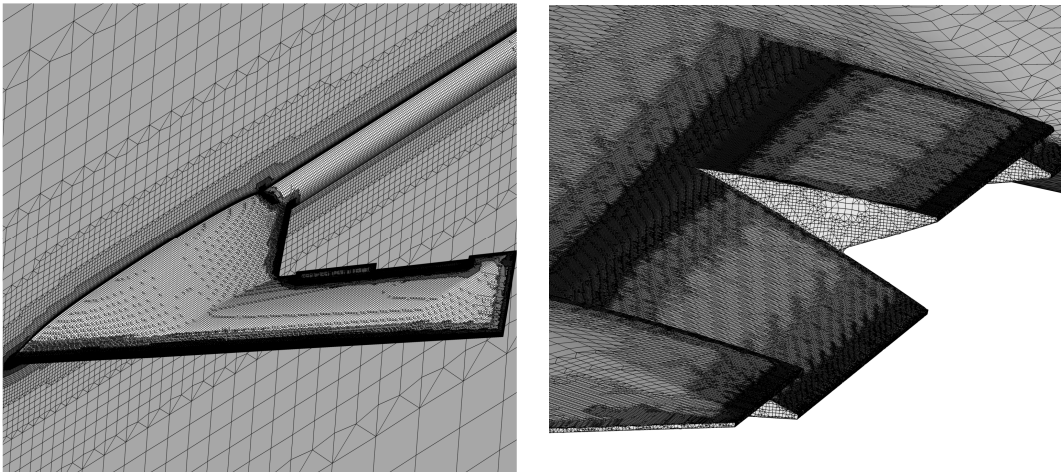


Figure 7: BOXERMesh grid for crow flaps

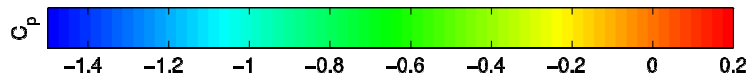


Figure 8: C_p Color bar for flow visualization, applies to figures 10, 12, 14, 16, 18, 20 and 22

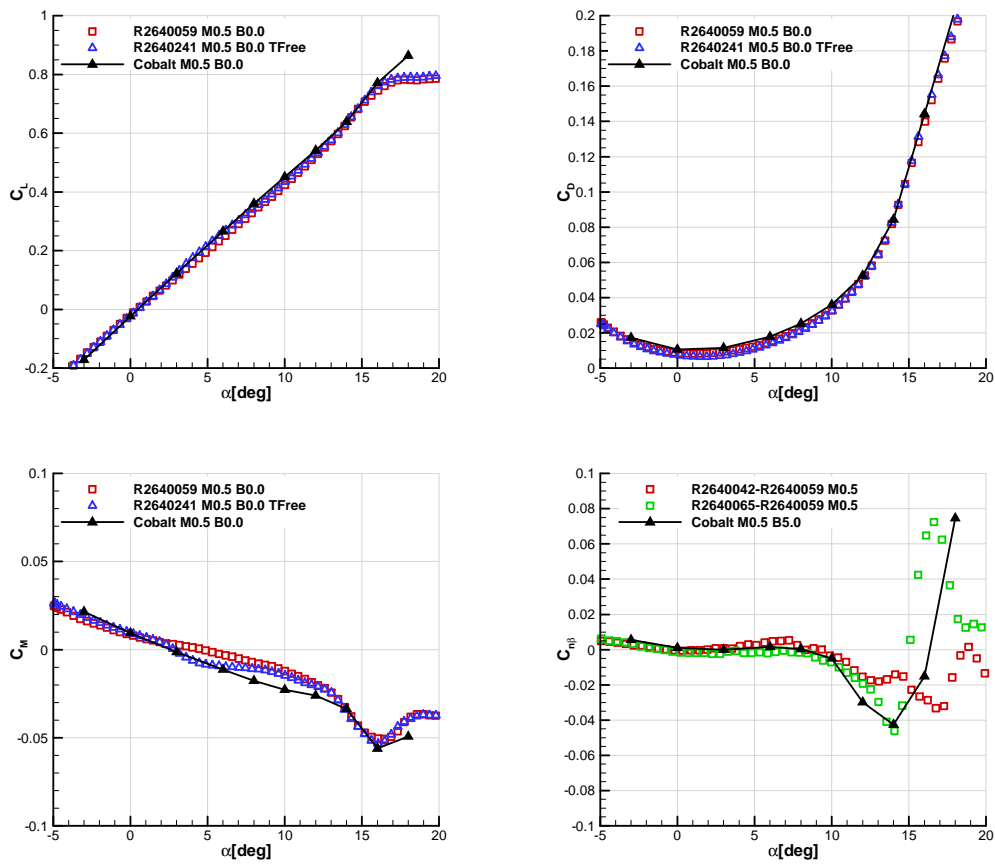


Figure 9: Clean configuration forces and moments $M=0.5$

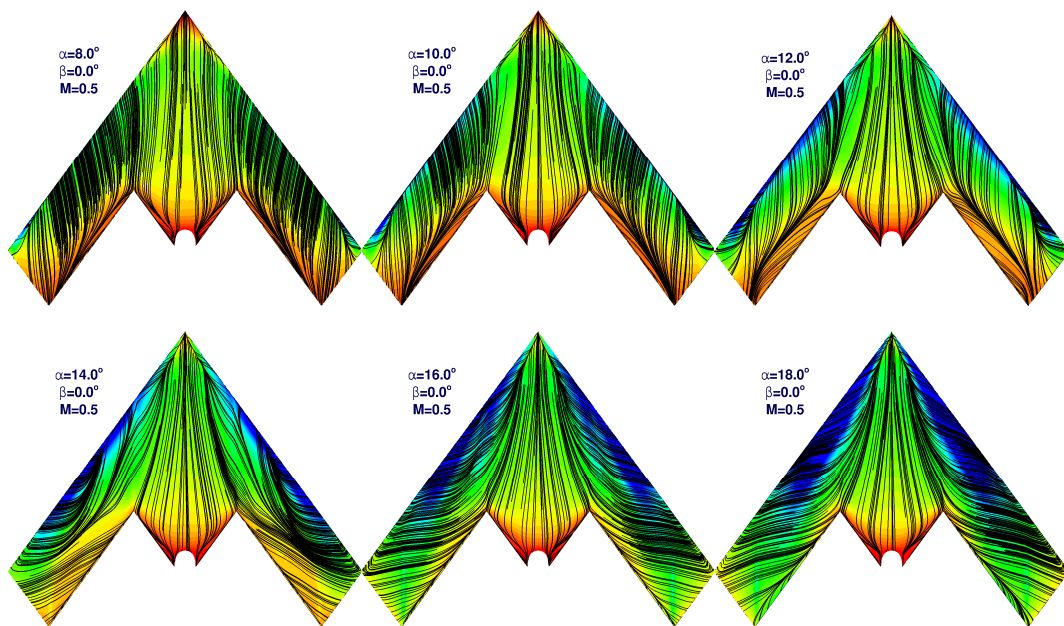


Figure 10: Clean configuration flow visualization $M=0.5$, C_p and skin friction streamlines

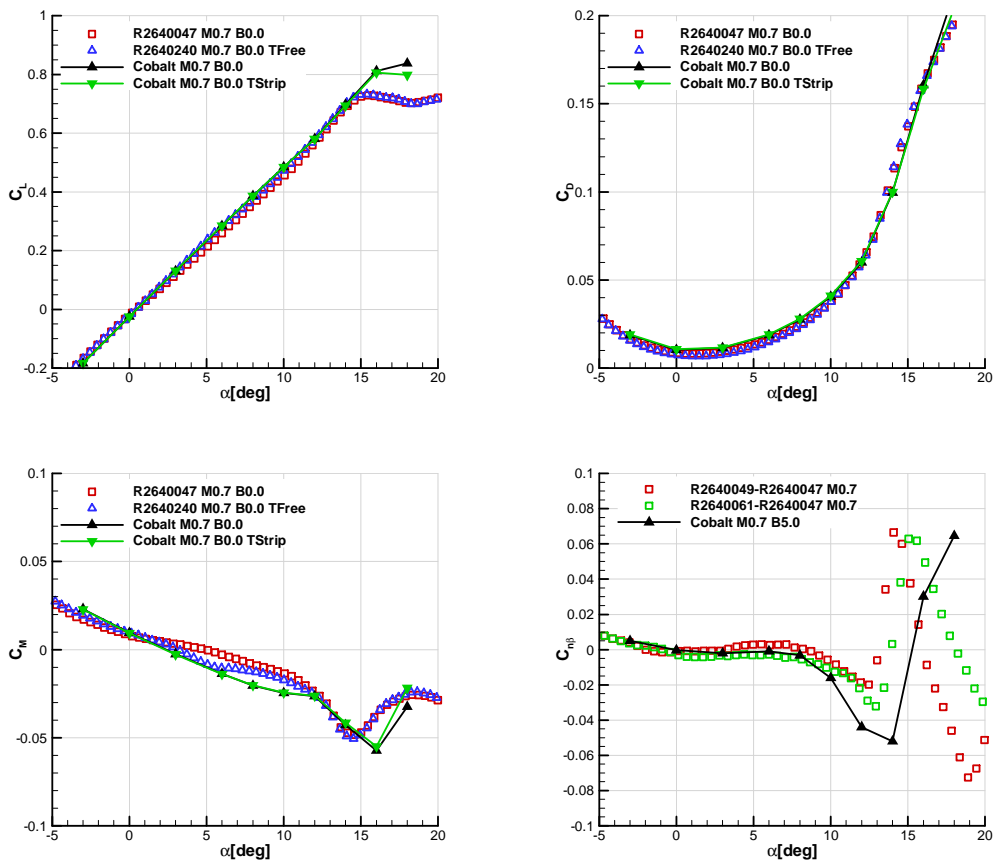


Figure 11: Clean configuration forces and moments $M=0.7$

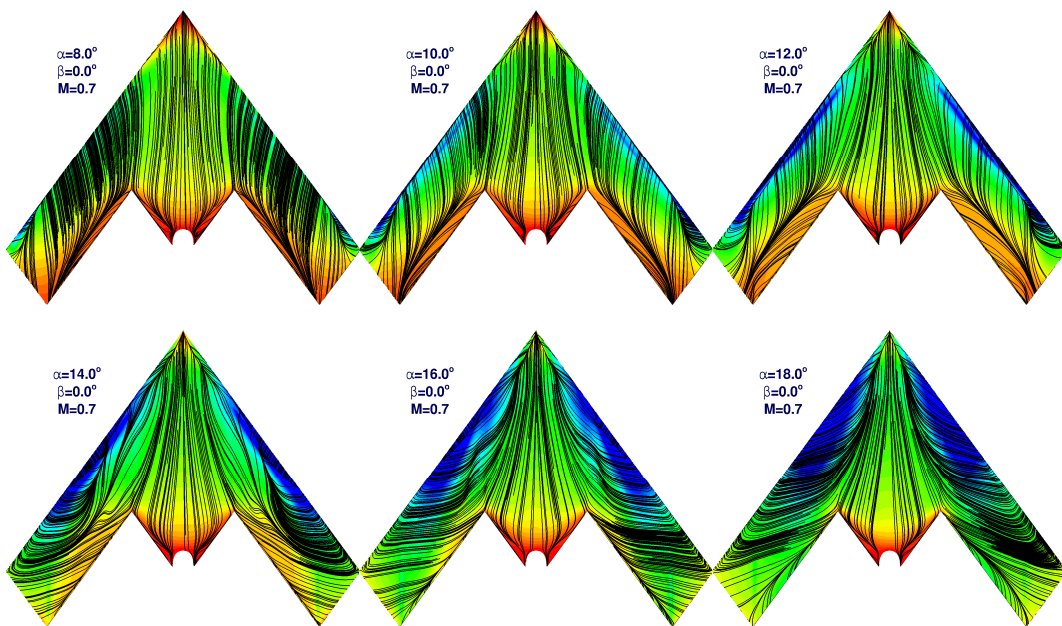


Figure 12: Clean configuration flow visualization $M=0.7$, C_p and skin friction streamlines

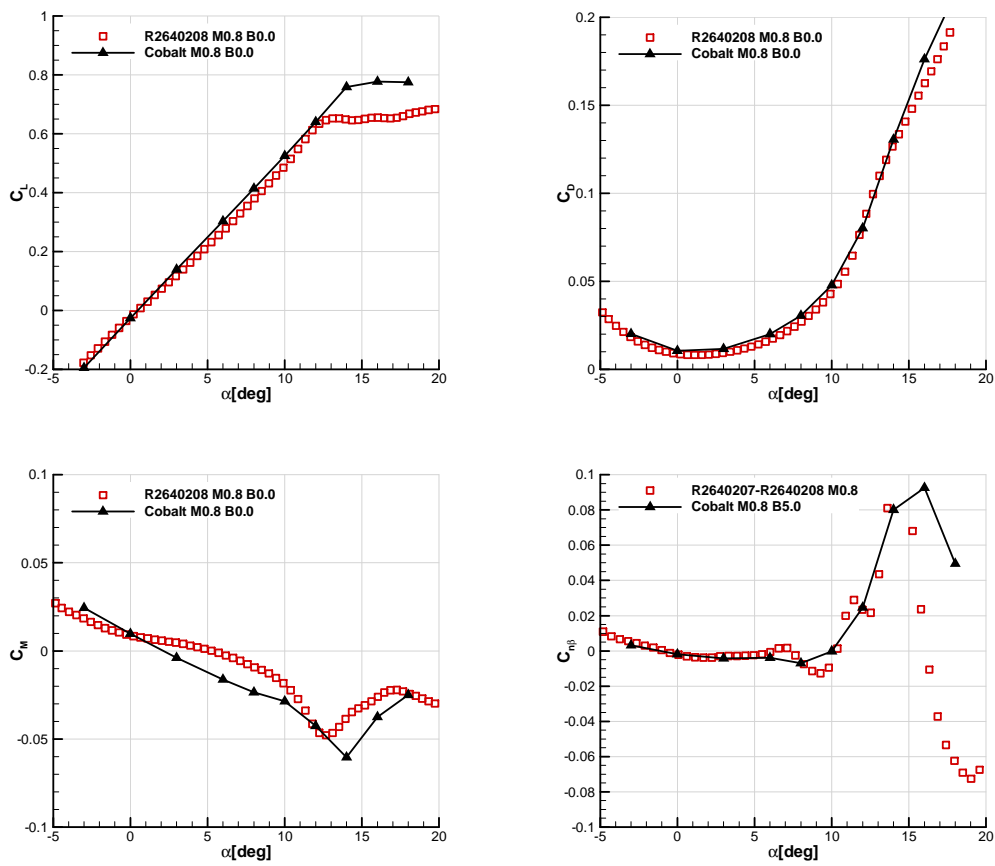


Figure 13: Clean configuration forces and moments $M=0.8$

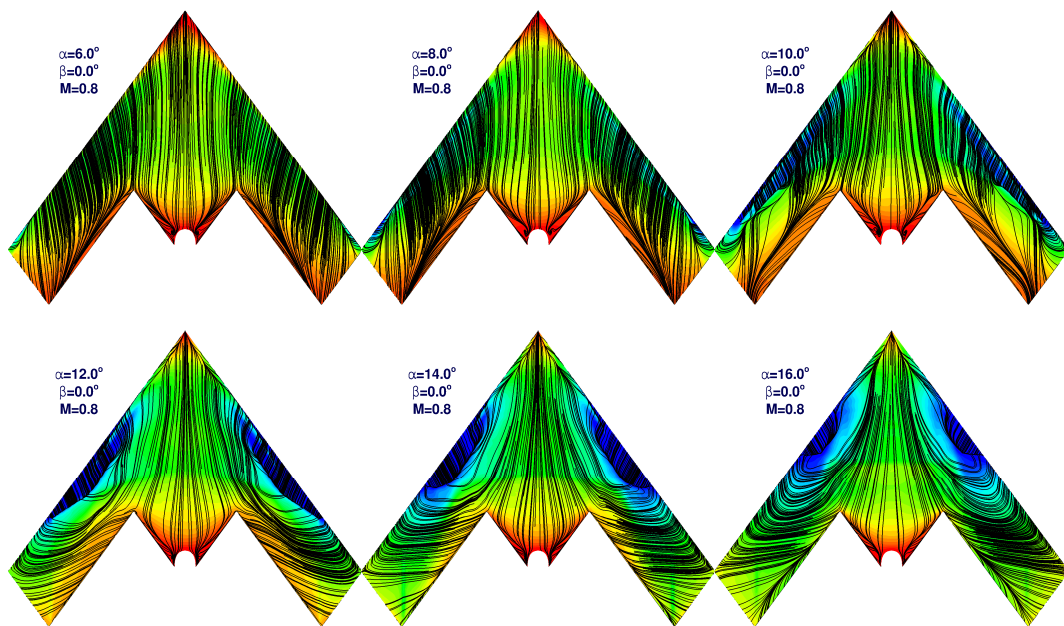


Figure 14: Clean configuration flow visualization $M=0.8$, C_p and skin friction streamlines

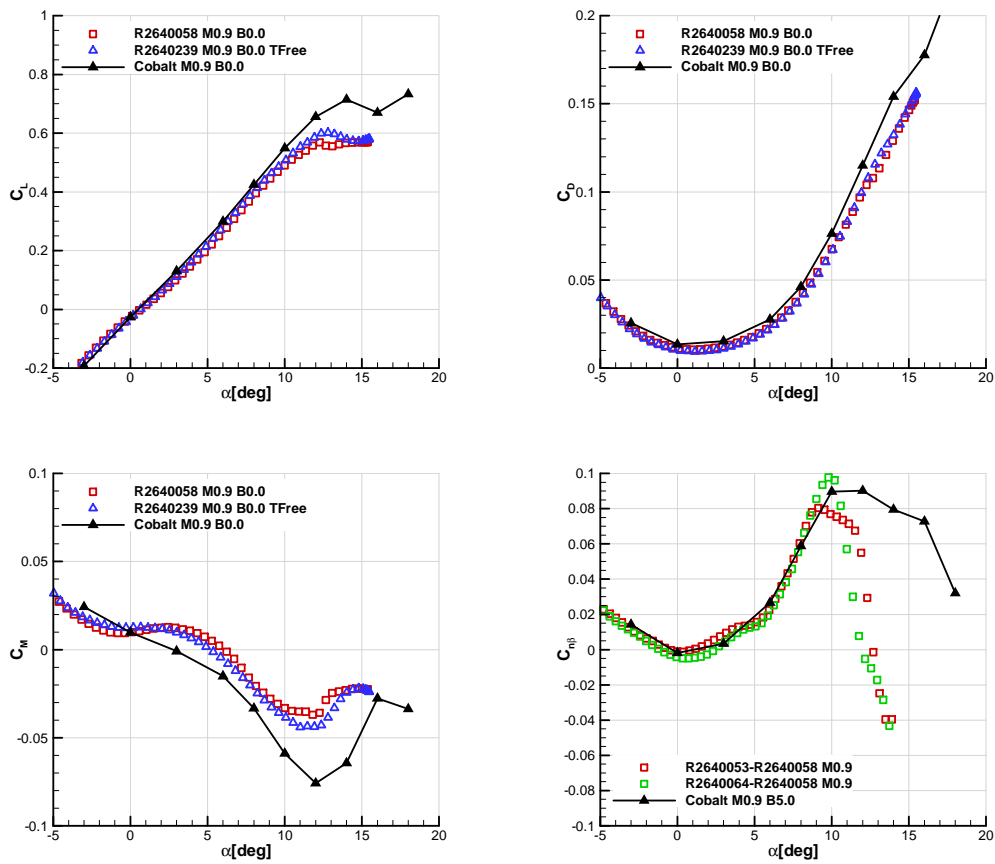


Figure 15: Clean configuration forces and moments $M=0.9$

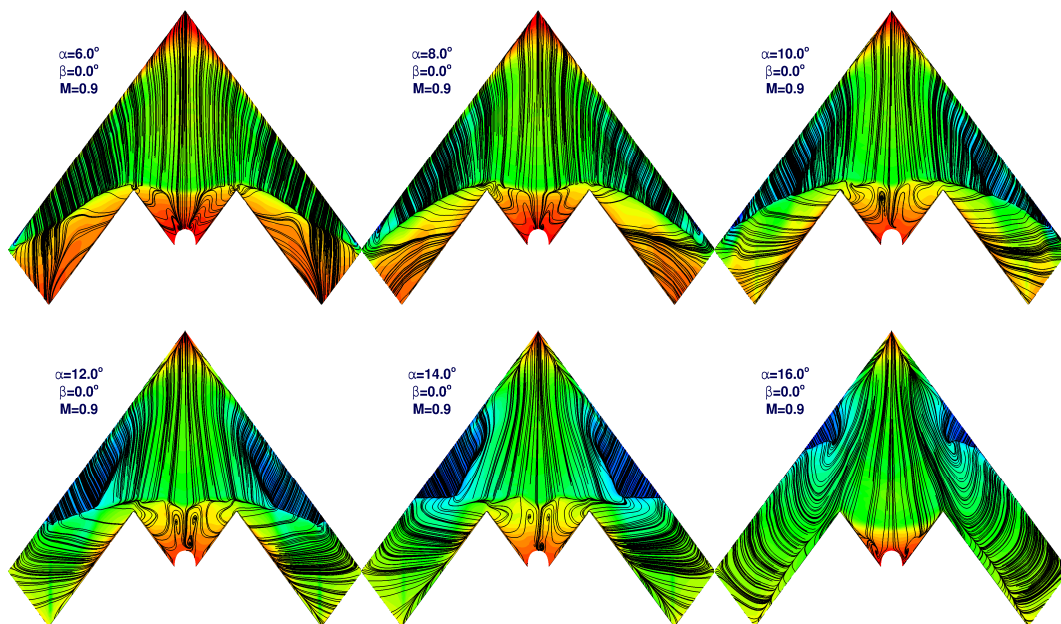


Figure 16: Clean configuration flow visualization $M=0.9$, C_p and skin friction streamlines

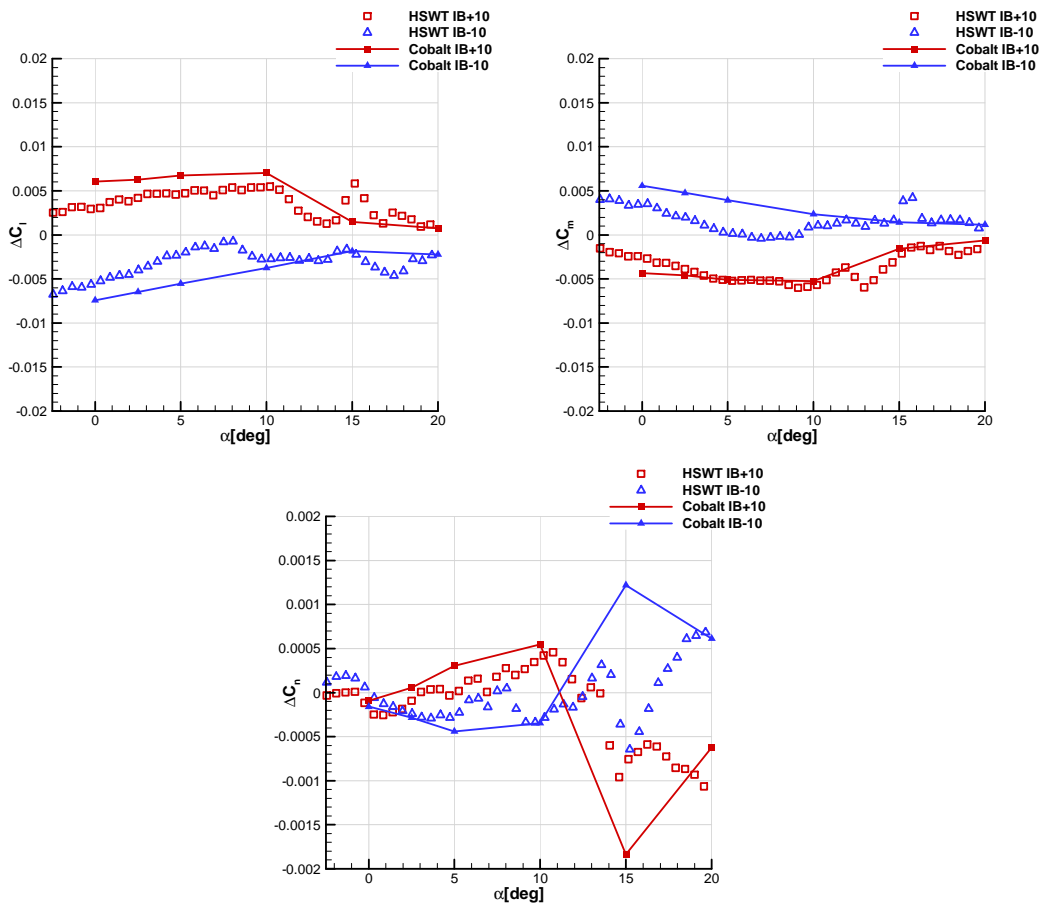


Figure 17: Inboard flaps (config 1, config 2) incremental forces

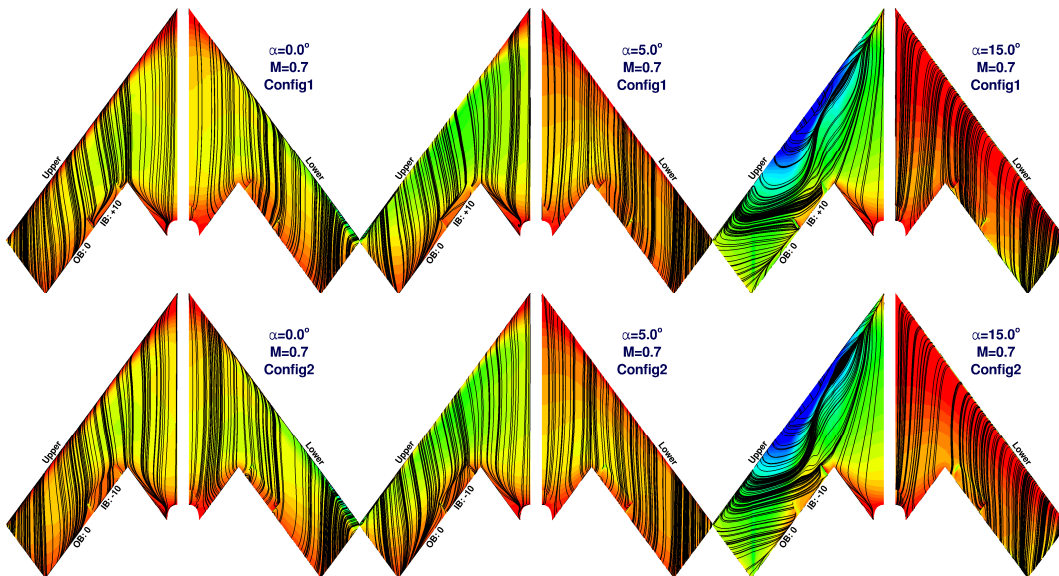


Figure 18: Inboard flaps (config 1, config 2) flow visualization, C_p and skin friction streamlines

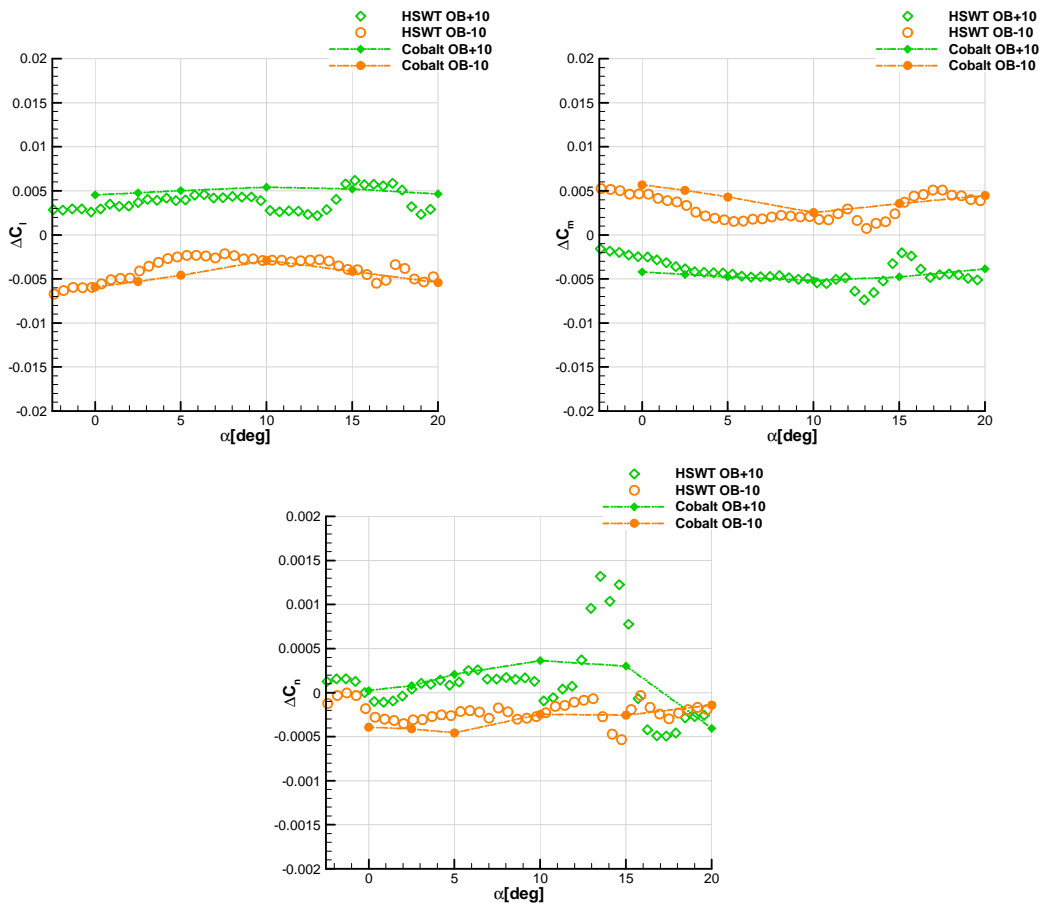


Figure 19: Outboard flaps (config 3, config 4) incremental forces

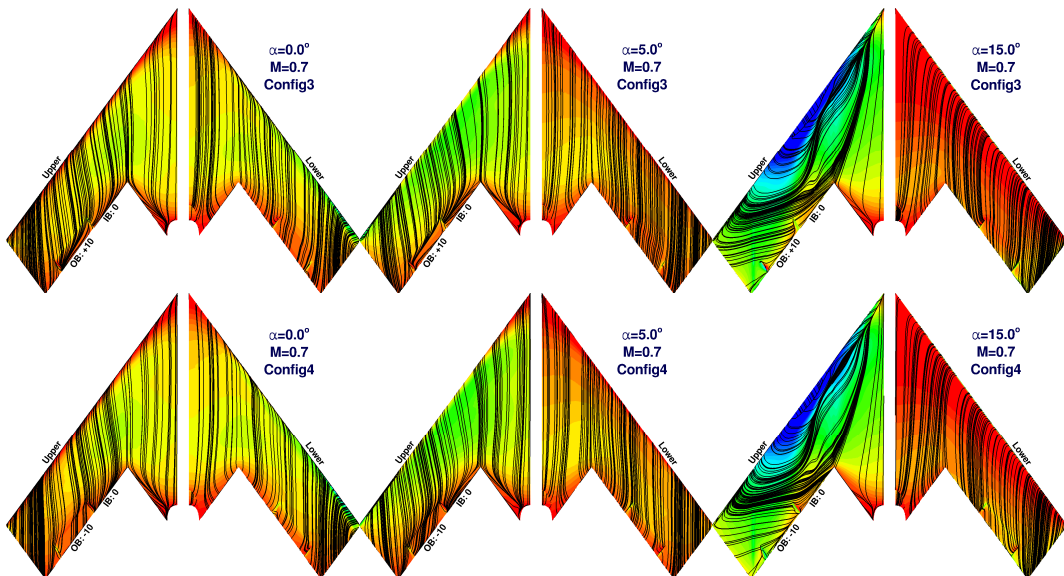


Figure 20: Outboard flaps (config 3, config 4) flow visualization, C_p and skin friction streamlines

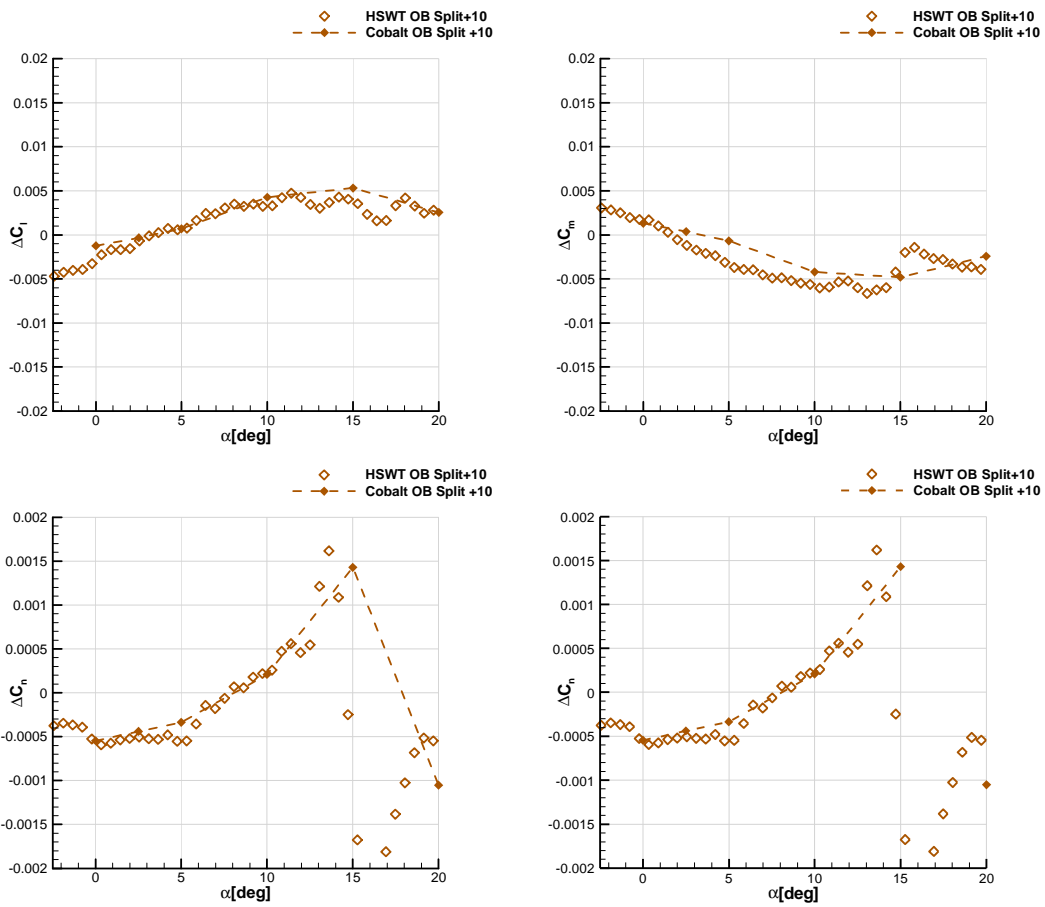


Figure 21: Split flap (config 5) incremental forces

1

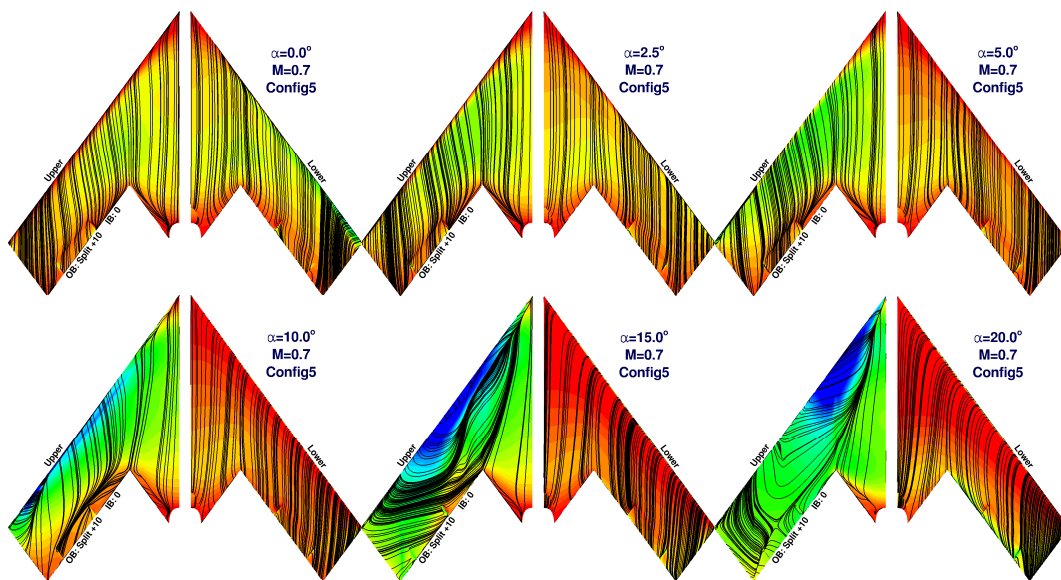


Figure 22: Split flap (config 5) flow visualization, C_p and skin friction streamlines

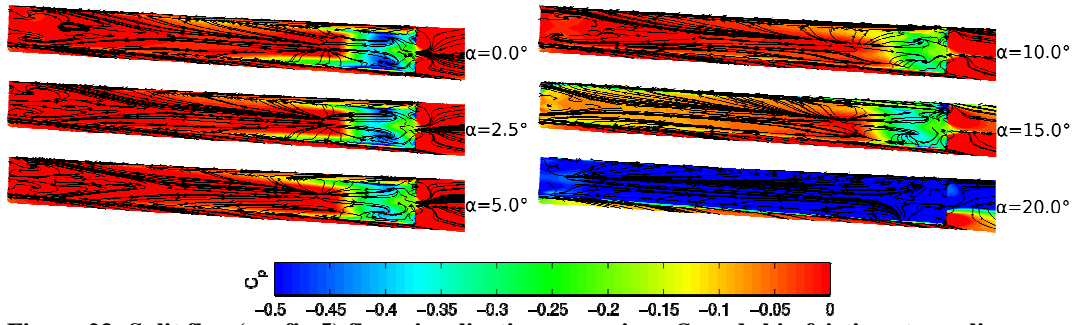


Figure 23: Split flap (config 5) flow visualization, rear view, C_p and skin friction streamlines

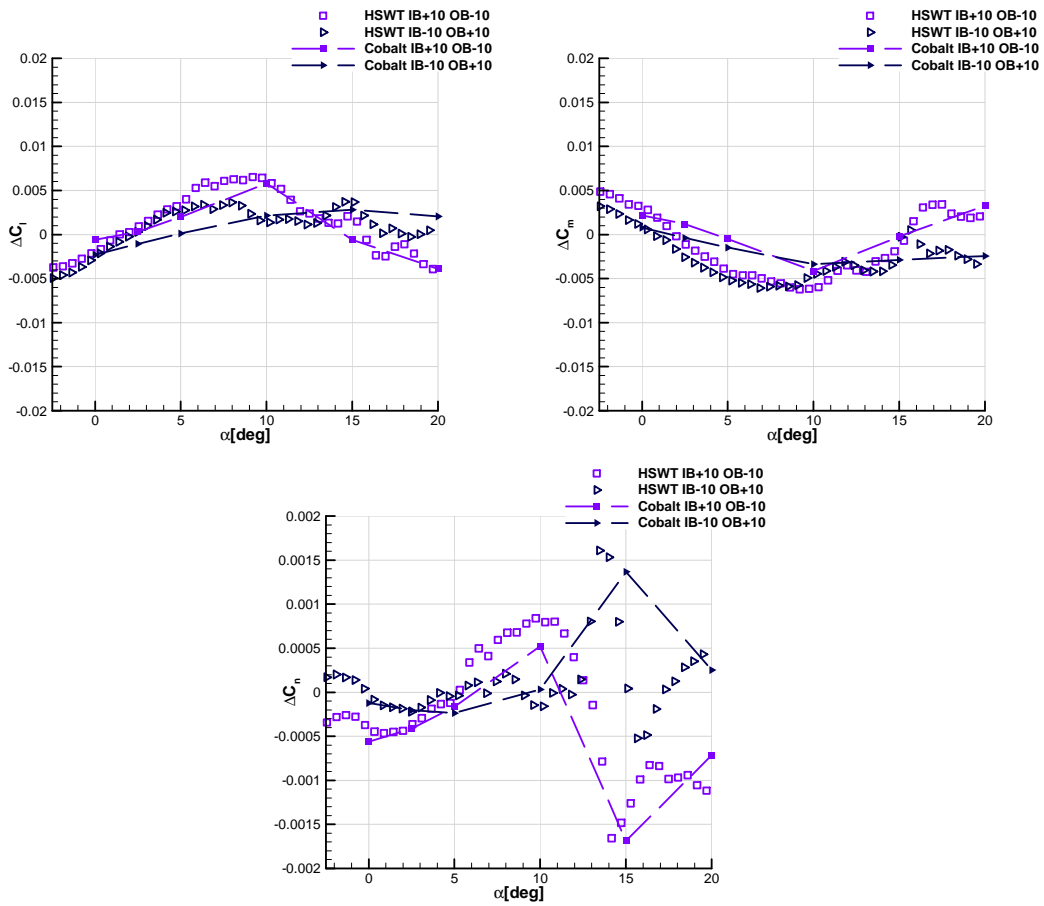


Figure 24: Crow flaps (config 6, config 7) incremental forces

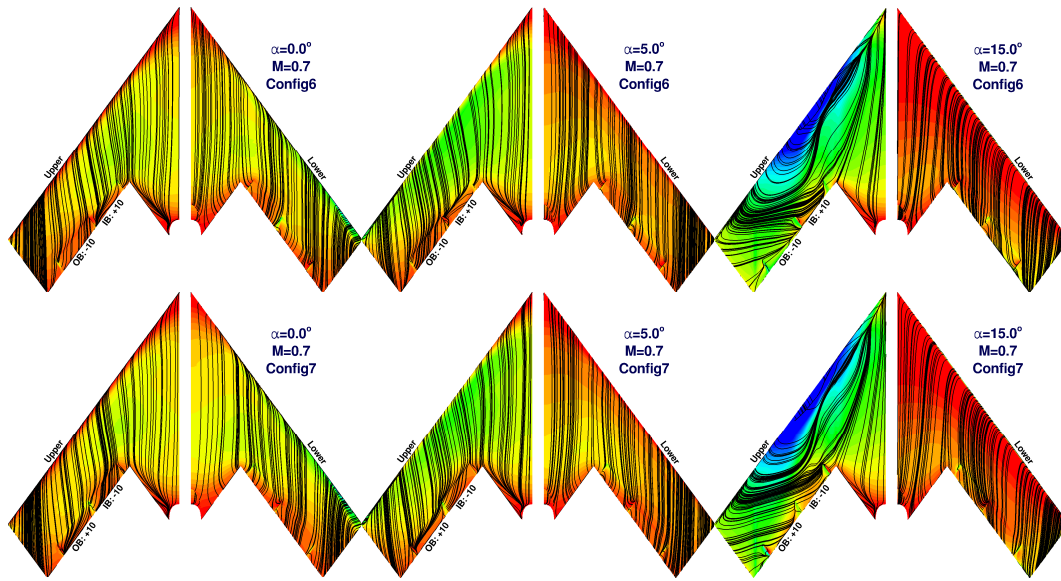


Figure 25: Crow flaps (config 6, config 7) flow visualization, C_p and skin friction streamlines

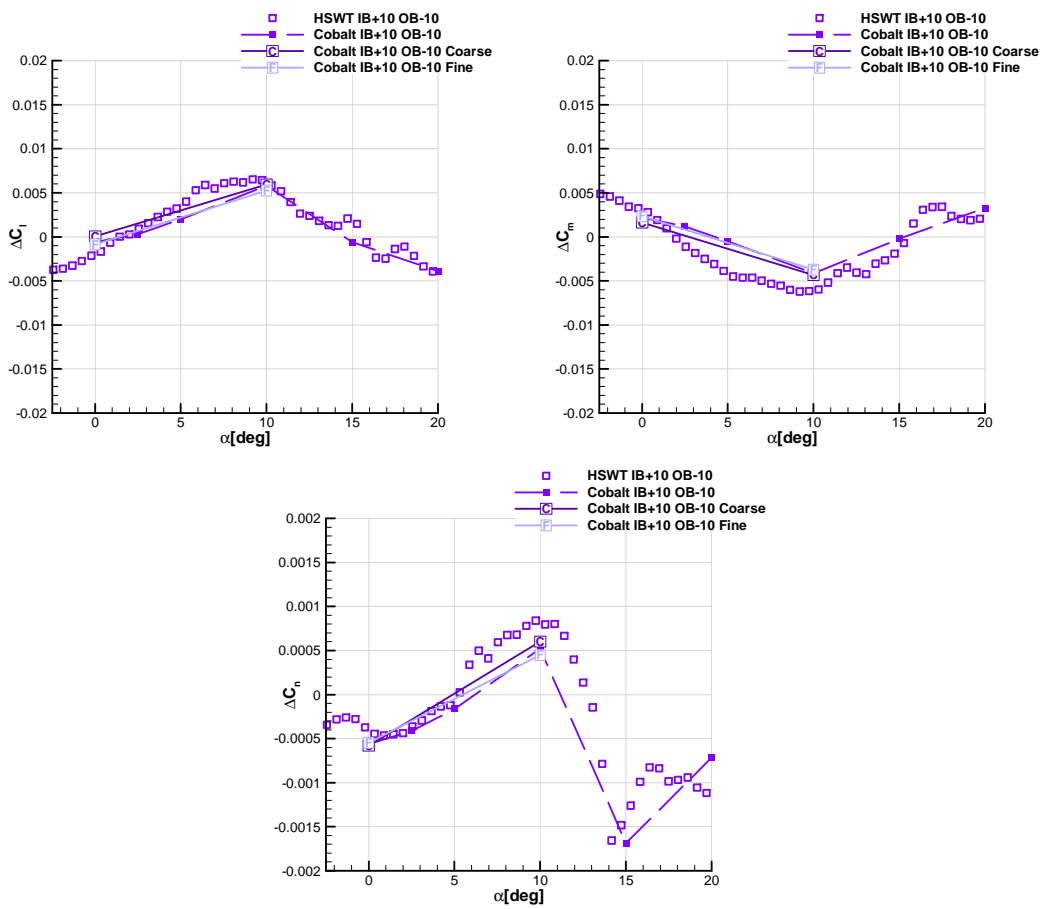


Figure 26 Crow flaps (config 6) mesh refinement incremental forces